Supporting Information for

Record Quantum Tunneling Time in an Air-Stable Exchange-Bias Dysprosium Macrocycle

Zhenhua Zhu,[†] Sagar Paul,*[,‡] Chen Zhao,[†] Jianfeng Wu,[§] Xu Ying,[†] Liviu Ungur,*[,¶] Wolfgang Wernsdorfer,[‡] Franc Meyer[‖] and Jinkui Tang*[,†,⊥]

[†]State Key Laboratory of Rare Earth Resource Utilization, Changchun Institute of Applied Chemistry, Chinese Academy of Sciences, Changchun 130022, P. R. China. E-mail: tang@ciac.ac.cn

[‡]Physikalisches Institut, Karlsruhe Institute of Technology (KIT), Engesserstraße 15, D-76131, Karlsruhe, Germany. E-mail: sagar.paul@kit.edu

[§]School of Chemistry and Chemical Engineering, Northwestern Polytechnical University, Xi'an 710072, P. R. China.

[¶]Department of Chemistry, National University of Singapore, 3 Science Drive 3, Singapore 117543, Singapore. Email: chmlu@nus.edu.sg

[‖]Institut für Anorganische Chemie, Universität Göttingen, Tammannstraße 4, D-37077 Göttingen, Germany.

[⊥]School of Applied Chemistry and Engineering, University of Science and Technology of China, Hefei 230026, P. R. China.

Contents

1. Synthesis and characterization

General procedure

All chemicals and solvents were obtained commercially and used as received without any further purification. 3,5-diacetyl-4-methyl-1-*H*-pyrazole was synthesized following a previously reported method.[1] The precursor **Dy_2^*Cl** was synthesized by *in situ* imine condensation reaction of 3,5-diacetyl-4-methyl-1*H*-pyrazole and *N*, *N*-bis(2-aminoethyl)methylamine in the presence of $DyCl_3 \cdot 6H_2O$ according to a previously published method.[2] Elemental analyses for C, H, N and S were performed on a Perkin-Elmer 2400 analyzer. FT-IR spectra were recorded with a Nicolet 6700 Flex FTIR spectrometer equipped with a smart iTR attenuated total reflectance (ATR) sampling accessory in the range from 4000 to 530 cm^{-1}. Powder X-ray diffraction (PXRD) measurements were recorded on Bruker D8 advance X-ray diffractometer using Cu-Kα radiation. Thermogravimetric analyses were recorded on a Netzsch STA449F3 TG-DSC instrument in the temperature range of 25-800 °C with a heating rate of 10 K min^{-1} under N_2 conditions.

Synthesis of **Dy_2**

Et_3N (0.6 mmol, 84 μL) and precursor **Dy_2^*Cl** (0.1 mmol, 95.9 mg) were added to a DCM/H_2O (20 mL/20 mL) solution of 4-(methylthio)phenol at room temperature. Then the mixture was refluxed for 1 hour. After cooling to room temperature, DCM phase was separated. Yellow crystals of **1** suitable for single crystal X-ray measurement were obtained by slow diffusion of n-pentane into DCM. Yield = 20% (based on Dy). Elemental analysis (%) calcd for $C_{54}H_{68}Dy_2N_{10}O_4S_4$ (M_w = 1374.42): C, 47.19; H, 4.99; N, 10.19; S, 9.33. Found: C, 47.01; H, 4.99; N, 10.15; S, 9.18. FTIR ν/cm^{-1} (ART): 2997 (w), 2917 (w), 1614 (s), 1582 (m), 1482 (s), 1431 (m), 1296 (vs), 1254 (m), 1212 (m), 1161 (w), 1123 (w), 1094 (m), 1043 (w), 965 (m), 856 (m), 828 (s), 775 (m), 719 (m), 659 (s), 543 (m).

Synthesis of **Dy_2@Y_2**

The precursor **Y_2^*Cl** was firstly synthesized by the same procedure to **Dy_2^*Cl** except that $YCl_3 \cdot 6H_2O$ was used instead of $DyCl_3 \cdot 6H_2O$. Then, **Y_2** was prepared using the same method to **Dy_2** except that the precursor **Y_2^*Cl** was used rather than **Dy_2^*Cl**. The crystalline samples **Y_2** (0.095 mmol, 116.59 mg) and **Dy_2** (0.005 mmol, 6.87 mg) were dissolved in DCM (100 mL) giving a clear solution. **Dy_2@Y_2** was obtained as yellow powders after removing DCM under a reduced pressure.

Synthesis of **DyY**

The precursor **DyY^*Cl** was synthesized using a same method to **Dy_2^*Cl** except that $DyCl_3 \cdot 6H_2O$ and $YCl_3 \cdot 6H_2O$ are used in a molar ratio of 1 to 19 instead of pure $DyCl_3 \cdot 6H_2O$. The synthesis of **DyY** was the same as that for **Dy_2**, except that the precursor **DyY^*Cl** was used to replace **Dy_2^*Cl**.

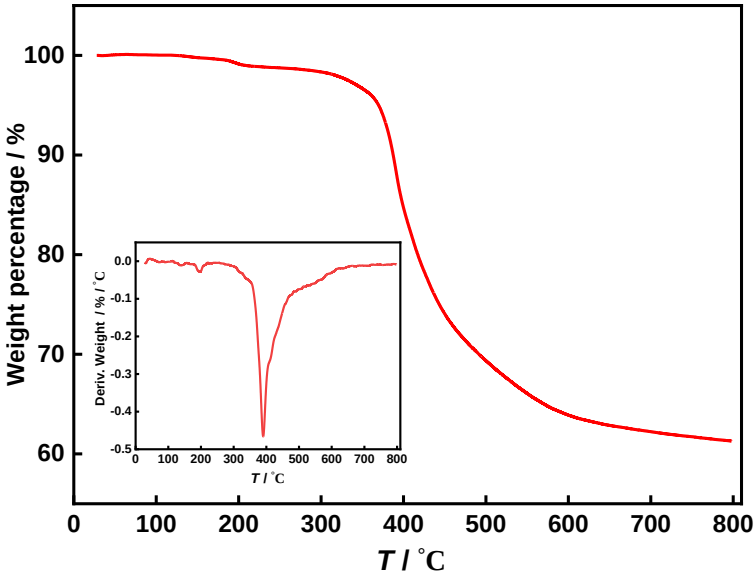

Figure S1. Thermogravimetric analysis of **Dy2**.

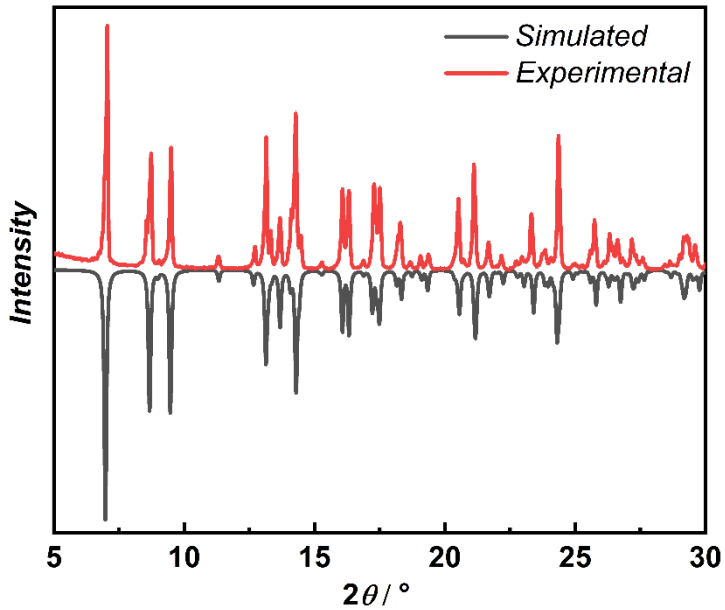

Figure S2. Experimental and simulated powder X-ray diffraction (PXRD) patterns of **Dy2**. The simulated pattern is calculated based on the single crystal X-ray diffraction structural model.

2. X-ray crystallography

Crystallographic data were collected using a Bruker SMART APEX diffractometer equipped with graphite-monochromatized Mo Kα radiation (λ = 0.71073 Å) at 180 K. The structures were determined in Olex2 with SHELXT structure solution program using intrinsic phasing solution method. The model was refined with SHELXL using least squares minimization.[3-5] All non-hydrogen atoms were refined anisotropically. All hydrogen atom positions were calculated geometrically and refined using the riding model. Crystallographic data and refinement details are given in Tables S1-S3.

Table S1. Crystal Data and Structure Refinement for **Dy2**.

Compound reference	**Dy2**
Chemical formula	$C_{54}H_{68}Dy_2N_{10}O_4S_4$
Formula Mass	1374.42
Temperature (K)	180.0
Crystal system	monoclinic
Space group	$P2_1/c$
a (Å)	13.4709(4)
b (Å)	15.4749(5)
c (Å)	14.3264(4)
α (°)	90
β (°)	112.0970(10)
γ (°)	90
Unit cell volume (Å^3)	2767.13(15)
Z	2
ρ_{calc} (g/cm^3)	1.650
μ / mm^{-1}	2.885
F (000)	1380.0
Radiation	MoKα (λ = 0.71073)
Reflections collected	29346
Independent reflections	4830
R_{int}	0.0243
GOF on F^2	1.243
R_1 ($I \geq 2\sigma$ (I))	0.0189
wR_2 (all data)	0.0426
CCDC number	2223798

Table S2. Crystal Data and Structure Refinement for **Y_2**.

Compound reference	**Y_2**
Chemical formula	$C_{54}H_{68}Y_2N_{10}O_4S_4$
Formula Mass	1227.24
Temperature (K)	180.0
Crystal system	monoclinic
Space group	$P2_1/c$
a (Å)	13.4581(5)
b (Å)	15.4761(6)
c (Å)	14.3076(6)
α (°)	90
β (°)	112.099(2)
γ (°)	90
Unit cell volume (Å^3)	2761.05(19)
Z	2
ρ_{calc} (g/cm^3)	1.476
μ / mm^{-1}	2.297
F (000)	1272.0
Radiation	MoKα (λ = 0.71073)
Reflections collected	21476
Independent reflections	4842
R_{int}	0.0332
GOF on F^2	1.031
R_1 ($I \geq 2\sigma$ (I))	0.0250
wR_2 (all data)	0.0632
CCDC number	2284417

Table S3. Selected bond distances (Å) for complexes **Dy_2**.

Dy_2	
Dy1−O1	2.1474(18)
Dy1−O2	2.1512(18)
Dy1−N1[1]	2.476(2)
Dy1−N2[1]	2.548(2)
Dy1−N3[1]	2.497(2)
Dy1−N4	2.473(2)
Dy1−N5	2.485(2)

[1]1−X, 1−Y, 1−Z

Table S4. Selected bond angles (°) for complexes **Dy$_2$**.

Dy$_2$	
O1−Dy1−O2	173.24(7)
O1−Dy1−N1^1	90.68(7)
O1−Dy1−N2^1	87.04(7)
O1−Dy1−N3^1	89.99(7)
O1−Dy1−N4	91.78(7)
O1−Dy1−N5	86.46(8)
O2−Dy1−N1^1	95.05(7)
O2−Dy1−N2^1	86.41(7)
O2−Dy1−N3^1	89.09(7)
O2−Dy1−N4	91.59(7)
O2−Dy1−N5	89.58(8)
N1^1−Dy1−N2^1	133.87(7)
N1^1−Dy1−N3^1	65.85(7)
N1^1−Dy1−N4	91.99(7)
N1^1−Dy1−N5	157.56(7)
N2^1−Dy1−N3^1	68.08(7)
N2^1−Dy1−N4	134.11(7)
N2^1−Dy1−N5	68.26(7)
N3^1−Dy1−N4	157.79(7)
N3^1−Dy1−N5	136.32(7)
N4−Dy1−N5	65.89(7)

^{1}1−X, 1−Y, 1−Z

Table S5. Selected bond distances (Å) for complexes **Y$_2$**.

Y$_2$	
Y1−O1	2.1442(14)
Y1−O2	2.1377(14)
Y1−N1	2.4625(16)
Y1−N2	2.4724(18)
Y1−N3^1	2.4873(17)
Y1−N4^1	2.4698(17)
Y1−N5^1	2.5435(17)

^{1}1−X, 1−Y, 1−Z

Table S6. Selected bond angles (°) for complexes **Y_2**.

Y_2	
O1−Y1−O2	173.09(2)
O1−Y1−N1	91.55(6)
O1−Y1−N2	89.52(6)
O1−Y1−N3[1]	89.24(6)
O1-Y1-N4[1]	94.94(6)
O1−Y1−N5[1]	86.35(6)
O2−Y1−N1	91.91(6)
O2−Y1−N2	86.42(6)
O2−Y1−N3[1]	89.85(6)
O2−Y1−N4[1]	90.96(6)
O2−Y1−N5[1]	86.96(6)
N1−Y1−N2	66.11(6)
N1−Y1−N3[1]	157.47(6)
N1−Y1−N4[1]	91.35(5)
N1−Y1−N5[1]	134.35(6)
N2−Y1−N3[1]	136.42(6)
N2−Y1−N4[1]	157.17(6)
N2−Y1−N5[1]	68.27(6)
N3[1]−Y1−N4[1]	66.15(5)
N3[1]−Y1−N5[1]	68.18(6)
N4−Y1−N5[1]	134.28(6)

[1]1−X, 1−Y, 1−Z

Table S7. The *CShM* values calculated by SHAPE 2.1 for **Dy$_2$**.[6-7]

Coordination Geometry	**Dy$_2$**
Heptagon (D_{7h})	32.306
Hexagonal pyramid (C_{6v})	22.373
Pentagonal bipyramid (D_{5h})	**1.121**
Capped octahedron (C_{3v})	8.694
Capped trigonal prism (C_{2v})	6.917
Johnson pentagonal bipyramid J13 (D_{5h})	2.354
Johnson elongated triangular pyramid J7 (C_{3v})	22.371

Table S8. The *CShM* values calculated by SHAPE 2.1 for **Y$_2$**.

Coordination Geometry	**Y$_2$**
Heptagon (D_{7h})	32.433
Hexagonal pyramid (C_{6v})	22.535
Pentagonal bipyramid (D_{5h})	**1.079**
Capped octahedron (C_{3v})	8.669
Capped trigonal prism (C_{2v})	6.901
Johnson pentagonal bipyramid J13 (D_{5h})	2.298
Johnson elongated triangular pyramid J7 (C_{3v})	22.570

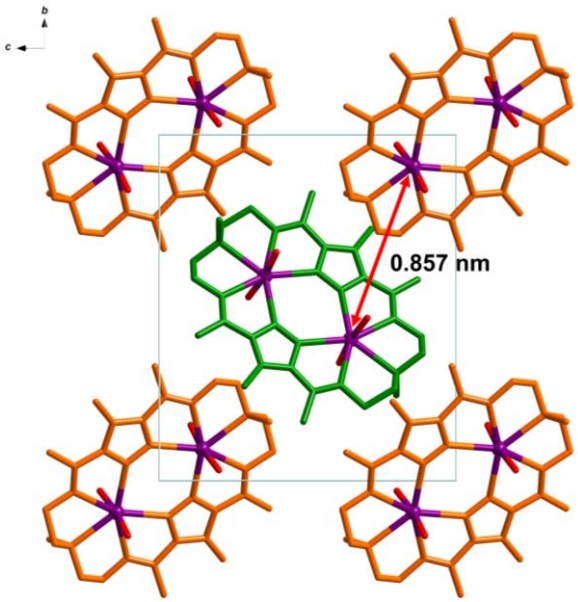

Figure S3. Packing diagram of **Dy$_2$** along *a* axis. The pale bule frame represents cell axes. The shortest intermolecular Dy···Dy distance is shown in a red double arrow.

3. Magnetic measurements

The magnetic measurements in the temperature range of 2 – 300 K were recorded on a Quantum Design MPMS-XL7 SQUID magnetometer (Figure S4-14, 17, 18; Table S9-10). Direct-current (dc) measurements were performed on fresh polycrystalline samples with an external magnetic field of 1000 Oe. Alternating-current (ac) measurements were performed at different frequencies from 0.1 to 1488 Hz under zero dc field and a 3.0 Oe ac oscillating field. The experimental magnetic susceptibilities were corrected for all the constituent atoms and the sample holder using Pascal's constants.[8] The dc decay measurements were collected by magnetizing the sample at 100 K using a dc field of 2 T, followed by removing the field and measuring the magnetization as a function of time.

In the temperature range of 30 mK - 4 K, the magnetization decay (Figure S15-16; Table S11) and the magnetic hysteresis loops (Figure S19), on a single crystal of **Dy2**, were obtained by μ-SQUIDs. After a fast sweep from saturation magnetization to zero field, the magnetization was plotted with waiting time to plot magnetization decay curves at zero field and different temperatures. Due to the different initial populations at different temperatures, the magnetization was normalized to initial population (N_0) to plot N/N_0 vs time (Figure S15). Figure S19 (top) shows the sweep rate dependent magnetic hysteresis curve at 30 mK obtained along the easy axis of the crystal. The observed four steps (Figure S19 top, middle), indicating QTM between the antiferromagnetic and ferromagnetic states, were tracked in the $M(H)$ curves obtained along different directions of field. This yields the derivative (dM/dH)-field angle map (Figure S19 bottom) that clearly shows the two axes in the crystal corresponding to the two macrocyclic planes (Figure S3).

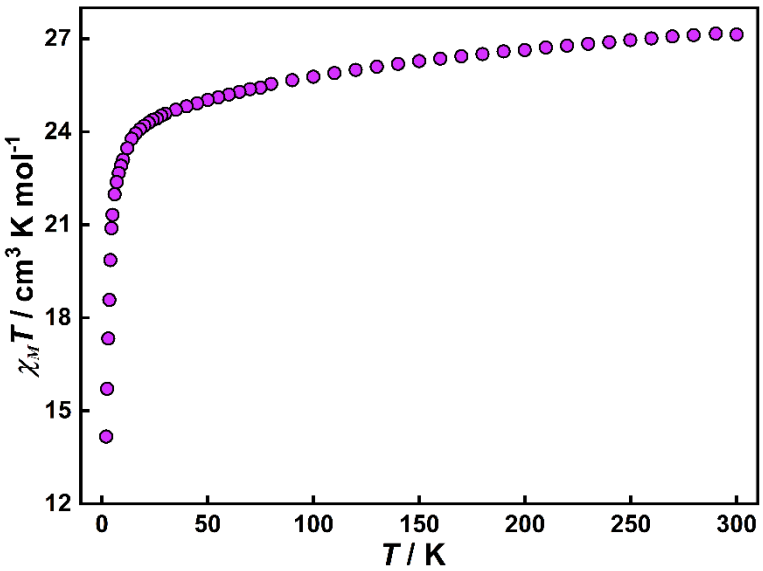

Figure S4. Plots of $\chi_M T$ versus temperature for **Dy2** under an applied magnetic field of 1000 Oe.

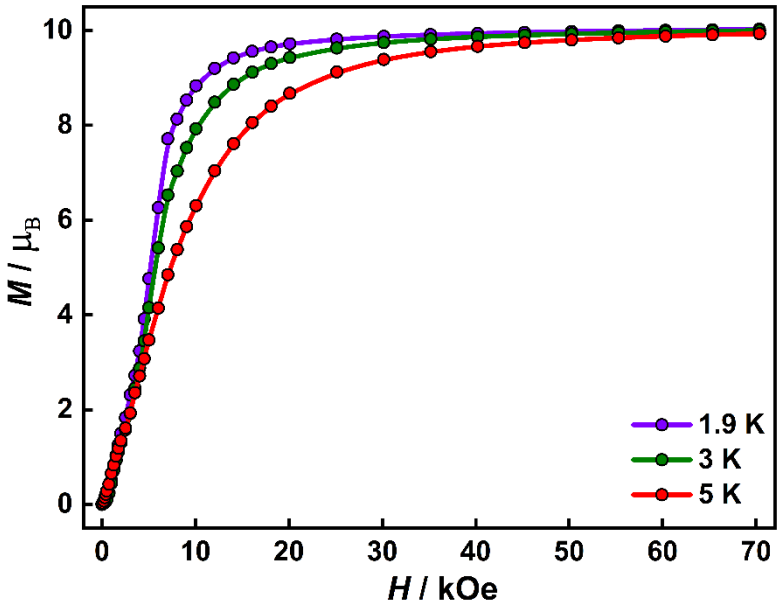

Figure S5. Field dependence of magnetization between 0 and 70 kOe and at temperatures of 1.9, 3.0, and 5.0 K for complex **Dy2**.

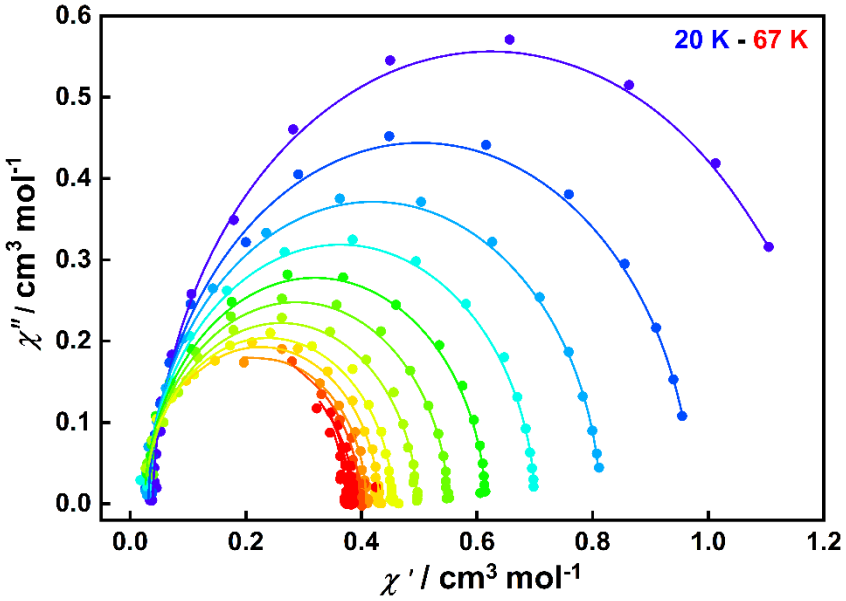

Figure S6. Cole-Cole plots for the ac susceptibilities for **Dy2** under zero dc field in the temperature range of 20 to 67 K. The solid lines represent the fitting results.

Table S9. The relaxation fitting parameters for **Dy_2** from fitting ac data at varying temperatures.

T (K)	χ_S	χ_T	τ	α
20	0.388638E-01	0.120735E+01	0.468268E-01	0.172481E-01
25	0.313664E-01	0.972531E+00	0.178550E-01	0.233623E-01
30	0.267766E-01	0.813683E+00	0.856665E-02	0.227608E-01
35	0.260249E-01	0.700565E+00	0.467174E-02	0.221357E-01
40	0.244613E-01	0.615009E+00	0.279405E-02	0.246432E-01
45	0.251584E-01	0.550243E+00	0.174044E-02	0.225359E-01
50	0.253361E-01	0.497065E+00	0.105991E-02	0.242130E-01
55	0.214525E-01	0.455393E+00	0.480640E-03	0.261966E-01
58	0.216882E-01	0.431013E+00	0.246654E-03	0.246996E-01
61	0.434133E-01	0.408348E+00	0.127005E-03	0.186612E-10
63	0.308753E-01	0.397476E+00	0.736453E-04	0.284973E-10
65	0.607967E-01	0.387165E+00	0.502963E-04	0.596823E-21
66	0.592774E-08	0.380521E+00	0.322772E-04	0.636871E-21
67	0.857422E-08	0.373858E+00	0.269987E-04	0.822618E-21

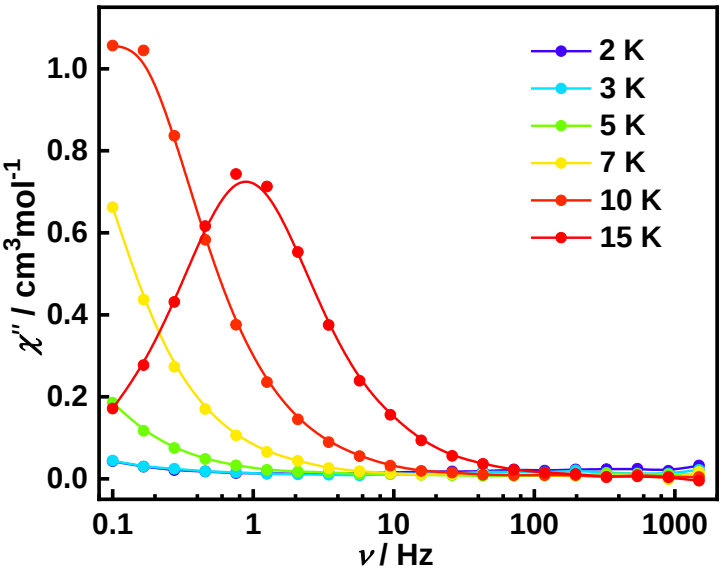

Figure S7. Frequency dependence of the out-of-phase susceptibility (χ'') for **Dy_2** under zero dc field in the temperature range of 2 to 15 K.

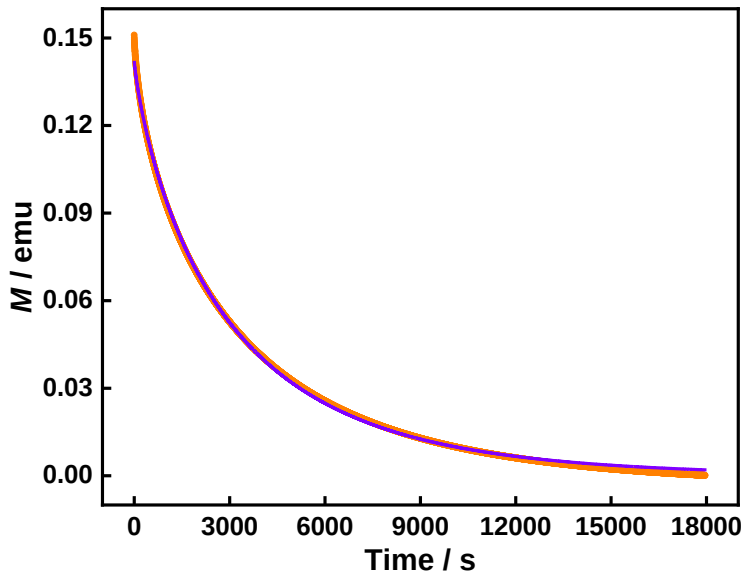

Figure S8. Plots of time-dependent decay of magnetization at 1.9 K for **Dy2**. The violet line represents the best fit using the following equation $M(t) = M_1 + (M_0 - M_1)\exp[-(t/\tau)^b]$, where M_0 is the initial magnetization after zero external field was achieved.

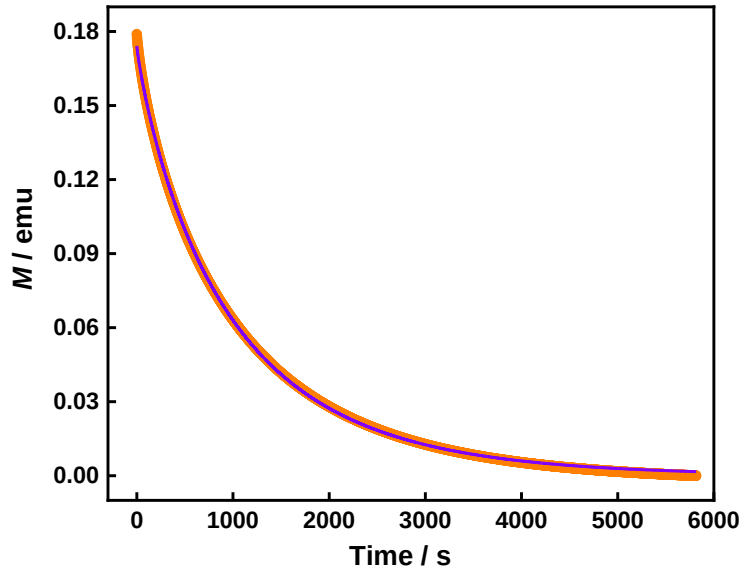

Figure S9. Plot of time-dependent decay of magnetization at 2.9 K for **Dy2**. The violet line represents the best fit using the following equation $M(t) = M_1 + (M_0 - M_1)\exp[-(t/\tau)^b]$, where M_0 is the initial magnetization after zero external field was achieved.

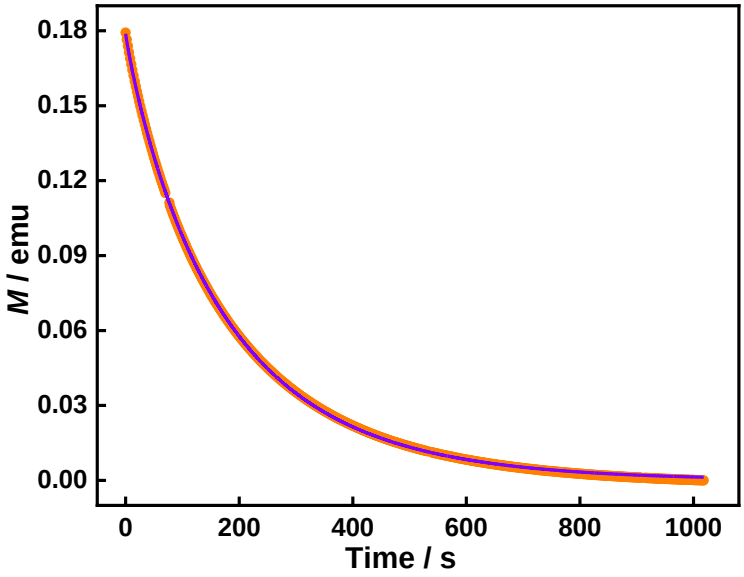

Figure S10. Plot of time-dependent decay of magnetization at 3.9 K for **Dy2**. The violet line represents the best fit using the following equation $M(t) = M_1 + (M_0 - M_1)\exp[-(t/\tau)^b]$, where M_0 is the initial magnetization after zero external field was achieved.

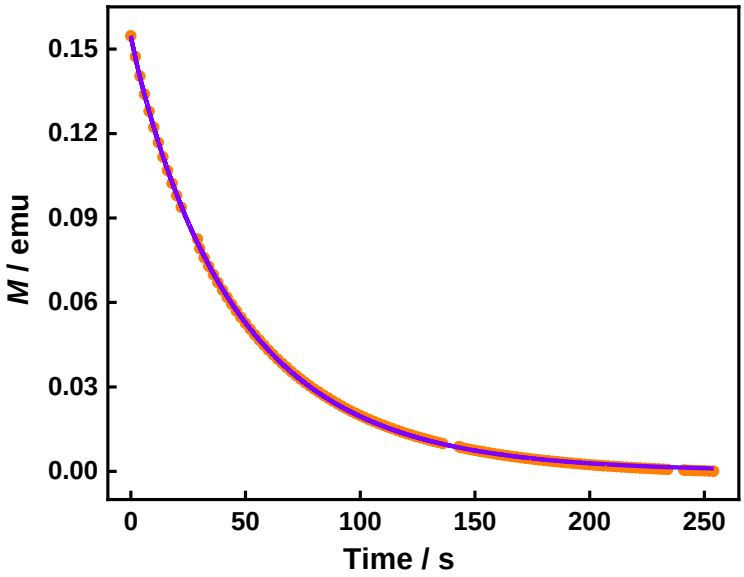

Figure S11. Plot of time-dependent decay of magnetization at 4.9 K for **Dy2**. The violet line represents the best fit using the following equation $M(t) = M_1 + (M_0 - M_1)\exp[-(t/\tau)^b]$, where M_0 is the initial magnetization after zero external field was achieved.

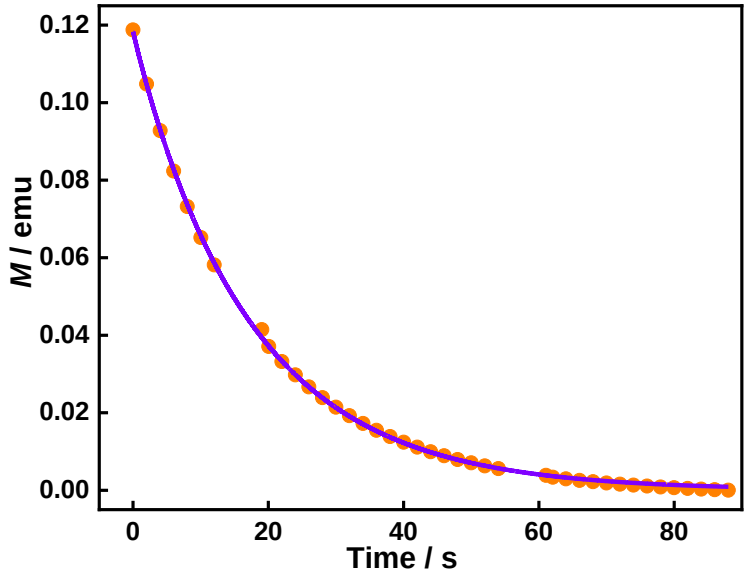

Figure S12. Plot of time-dependent decay of magnetization at 5.9 K for **Dy2**. The violet line represents the best fit using the following equation $M(t) = M_1 + (M_0 - M_1)\exp[-(t/\tau)^b]$, where M_0 is the initial magnetization after zero external field was achieved.

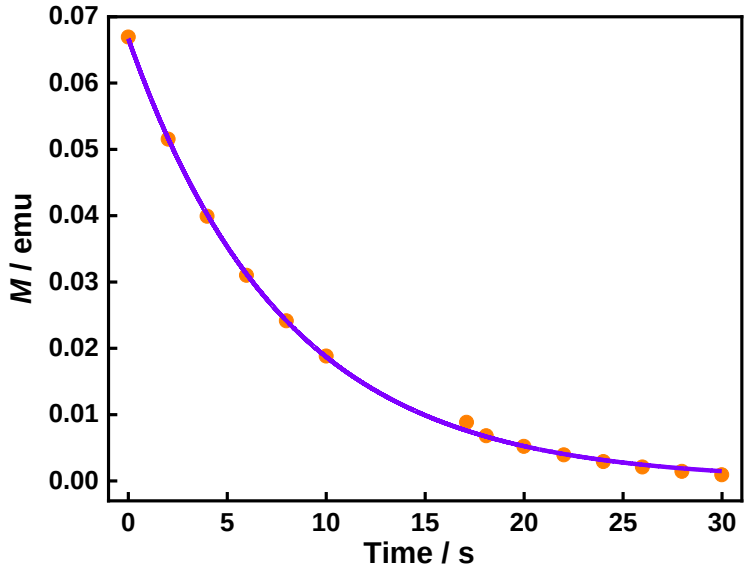

Figure S13. Plot of time-dependent decay of magnetization at 6.9 K for **Dy2**. The violet line represents the best fit using the following equation $M(t) = M_1 + (M_0 - M_1)\exp[-(t/\tau)^b]$, where M_0 is the initial magnetization after zero external field was achieved.

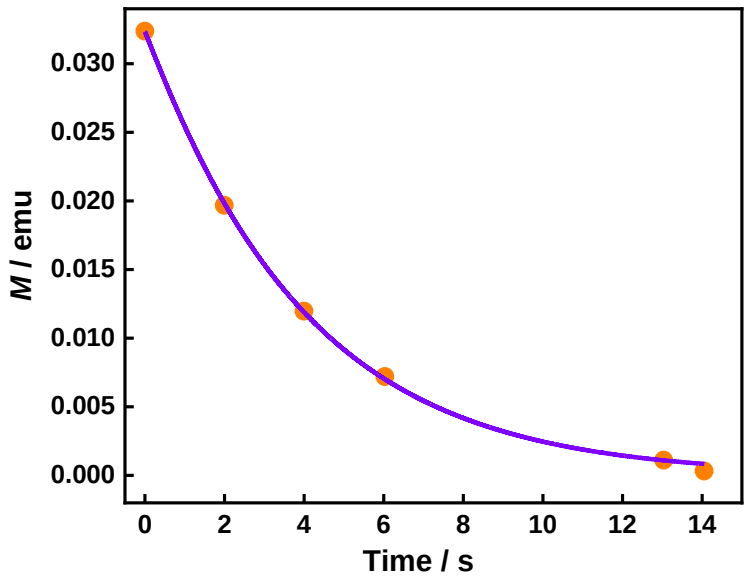

Figure S14. Plot of time-dependent decay of magnetization at 7.9 K for **Dy2**. The violet line represents the best fit using the following equation $M(t) = M_1 + (M_0 - M_1)\exp[-(t/\tau)^b]$, where M_0 is the initial magnetization after zero external field was achieved.

Table S10. Magnetic relaxation times extracted from dc magnetisation decay data for **Dy2**.

Temperature (K)	τ (s)
1.9	3016
2.9	980.7
3.9	174.5
4.9	46.28
5.9	17.25
6.9	7.864
7.9	3.997

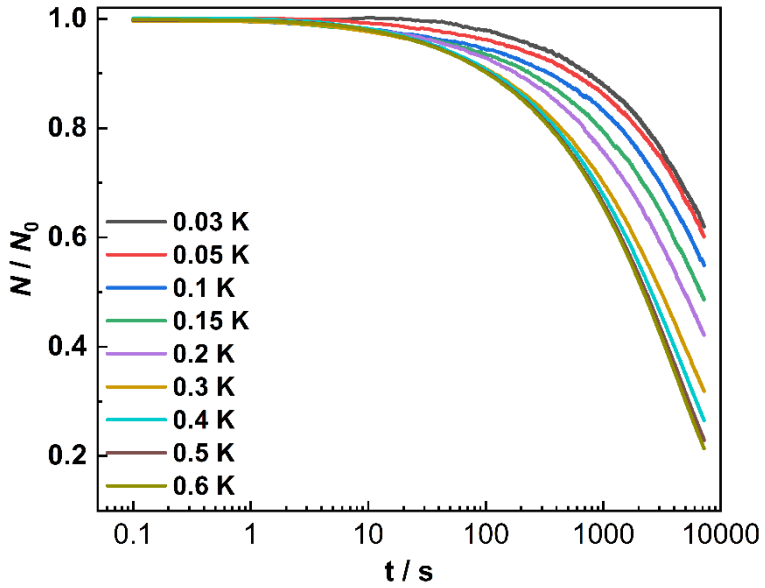

Figure S15. Magnetization vs. time decay plots for a single crystal of **Dy2** at the indicated temperatures.

Table S11. Magnetic relaxation times extracted from Figure S15 for **Dy$_2$**.

Temperature (K)	**τ (s)**
0.03	25601
0.05	23487.16
0.1	17655.86
0.15	12800.5
0.2	9309.455
0.25	6956.793
0.3	5689.111
0.4	4531.15
0.5	3908.55
0.6	3657.286

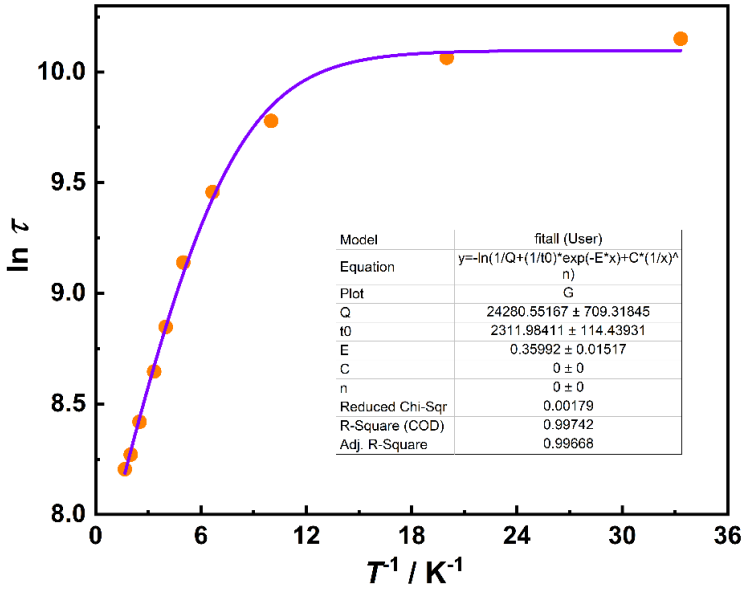

Figure S16. Temperature dependence of the relaxation time τ for **Dy$_2$** measured at low temperatures (0.03 - 0.6 K) by μ-SQUIDs. The solid lines are the fitting results using equation $\ln(\tau) = -\ln[(1/10\text{^}p_2) \exp(-E_2/k_BT) + 1/\tau_{QTM}]$.

Table S12. Some representative examples of high-performance dinuclear lanthanide SMMs highlighting the relaxation time of zero-field QTM.

Compound	U_{eff} / cm^{-1}	T_B / K	Sweep rate / Oe/s	τ_{QTM} / s	Ref.	Notes
$[Dy(Cy_3PO)_2(\mu\text{-}I)(I)_2]_2\cdot 4C_7H_8$	897	14	120	3.88×10^{-4}	9	Air-stable; Nonradical
$[Dy_2(BPA\text{-}TPA)_2(C_6H_4O_2)](BPh_4)_4\cdot 4CH_3CN$	505	20	200	4.45×10^{-2}	10	Air-stable; Nonradical
$[Dy(Cy_3PO)_2(\mu\text{-}Br)(Br)_2]_2\cdot 2C_7H_8$	476	3	8.7	1.69×10^{-3}	11	Air-stable; Nonradical
$Dy_2@C_{80}(CH_2Ph)$	426	21	29	3.25×10^{3}	12	Air-stable; Radical
$Tb_2@C_{80}(CH_2Ph)$	555	28	95	6.50×10^{4}	13	Air-stable; Radical
$Tb_2@C_{80}(CF_3)$	557	27	29	3.56×10^{4}	14	Air-stable; Radical
$Tb_2@C_{79}N$	526	26	29	1.66×10^{4}	15	Air-stable; Radical
$[K(crypt\text{-}222)(THF)][(Cp^{Me4H}{}_2Tb(THF))_2(\mu\text{-}N^{\cdot}{}_2)]$	242	15	100	3.64×10^{3}	16	Air-sensitive; Radical
$[K(crypt\text{-}222][(Cp^{Me4H}{}_2Tb)_2(\mu\text{-}N^{\cdot}{}_2)]$	276 / 564	30	100	4.00×10^{4}	16	Air-sensitive; Radical
$[K(crypt\text{-}222)][(Cp^{Me4H}{}_2Dy)_2(\mu\text{-}N^{\cdot}{}_2)]$	108	7.5	100	6.70×10^{2}	16	Air-sensitive; Radical
$[(Cp^{Me5}{}_2Dy)_2(\mu\text{-}5,5'\text{-}F_2bpym)](BPh_4)$	93	7	24	3.16×10^{2}	17	Air-sensitive; Radical
Dy_2	670	14.9	200	2.43×10^{4}	This work	Air-stable; Nonradical

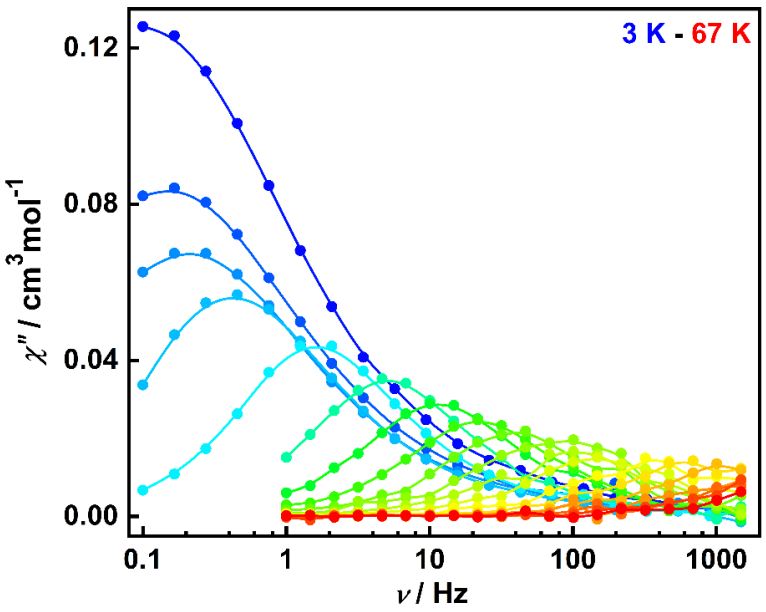

Figure S17. Frequency dependence of the out-of-phase susceptibility (χ'') for **DyY** under zero dc field in the temperature range of 3 to 67 K.

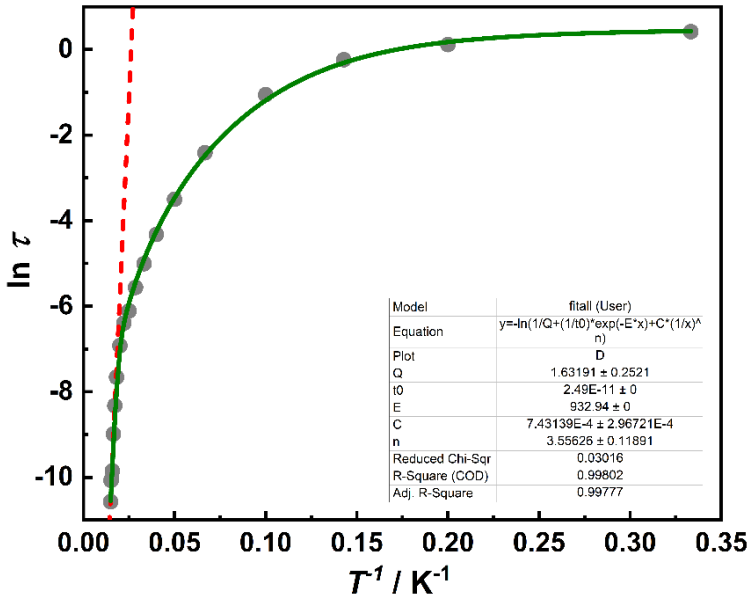

Figure S18. Temperature dependence of the relaxation time τ for **DyY**. The red and green lines are given by $\ln(\tau) = -\ln[\tau_0^{-1}\exp(-U_{eff}/k_BT]$ and $\ln(\tau) = -\ln[\tau_0^{-1}\exp(-U_{eff}/k_BT) + CT^n + 1/\tau_{QTM}]$, respectively.

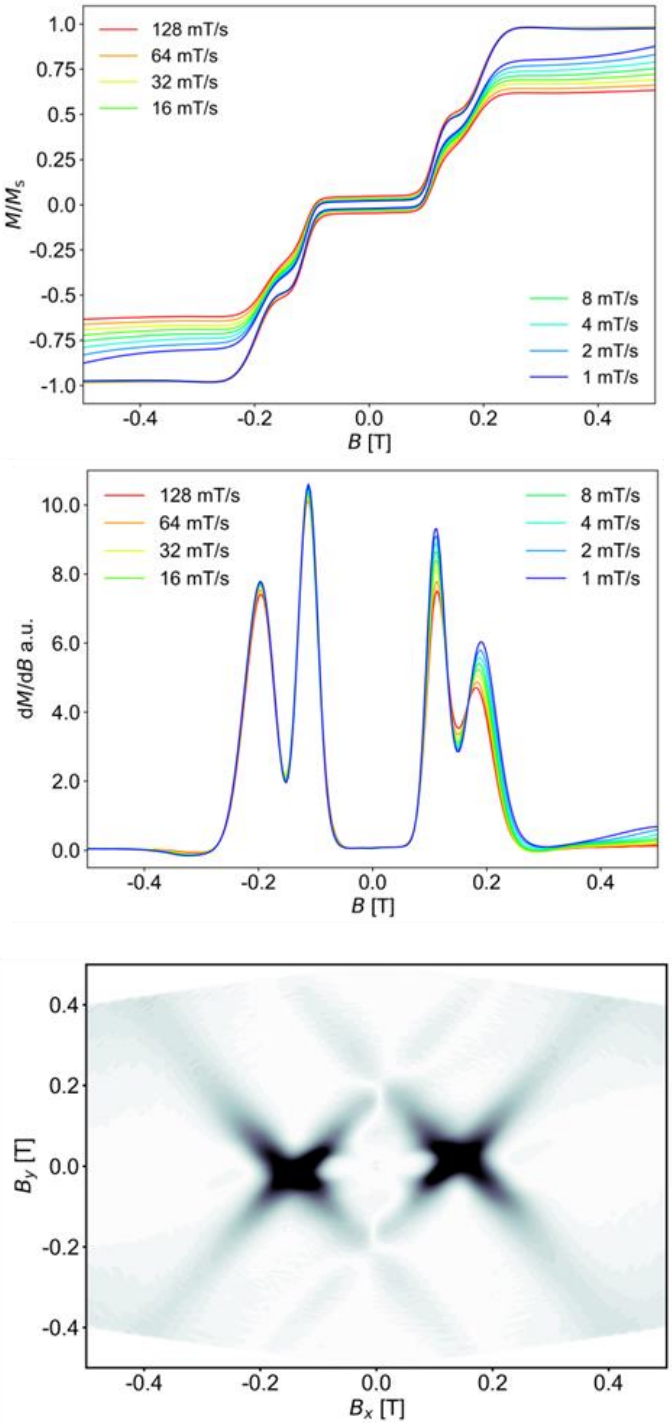

Figure S19. μ-SQUID measurements on a single crystal of **Dy_2**, normalized *M*(*H*) plots at 30 mK at various sweep rates (top) and the corresponding first-field derivative (d*M*/d*H*) (middle). Field angle dependent derivative (d*M*/d*H*) map (bottom) obtained from *M*(*H*) measured at different directions of field with respect to the crystal.

4. Ab initio calculations

Computational Details

The magnetic properties of **Dy$_2$** have been studied by standard ab initio calculations based on multiconfigurational methods.[18-19] The full molecular structure from single-crystal X-ray analysis was directly employed, i.e., no geometry optimization was done. All atoms were described with the ANO-RCC basis sets, which include relativistic corrections for core orbitals. Three different basis set definitions were employed, Dy(III) and all closely spaced atoms were described with large basis sets, while distant atoms were described with medium (smaller) basis.[20] To describe the low-lying local energy spectra of individual Dy(III) ion, the neighboring metal center was computationally modeled by diamagnetic Lu(III). The active space of the complete active space self-consisting field (CASSCF) of calculation of the Dy(III) included the $4f^9$ configuration (CAS (9 in 7) since only ligand field states are considered. 21 states with S = 5/2, 128 states with S = 3/2 and 130 states with S = 1/2 states were mixed by the spin-orbit interaction in RASSI. The local magnetic properties (g-tensors, main magnetic axes, crystal field parameters, etc.) were computed by the SINGLE_ANISO program based on the resulting spin-orbital multiplets. The magnetic properties of the entire complex, involving two Dy(III) centers, were calculated by the POLY_ANISO program, in which the anisotropic exchange interactions were simulated within the Lines model.

Table S13. *Ab initio* energy structure for the ground J =15/2 multiplet of one single Dy sites in **Dy$_2$**.

	Basis MB		**Basis VDZP**		**Basis VTZP**	
	Energy (cm^{-1})	Main values of the g-tensor	Energy (cm^{-1})	Main values of the g-tensor	Energy (cm^{-1})	Main values of the g-tensor
KD1	0.0 0.0	0.00039 0.00045 19.88053	0.0 0.0	0.00087 0.00108 19.87635	0.0 0.0	0.00071 0.00086 19.87891
KD2	512.7 512.7	0.01147 0.01517 16.97041	403.7 403.7	0.02472 0.03739 17.04089	437.0 437.0	0.02037 0.03009 17.03045
KD3	896.9 896.9	0.23254 0.26880 14.07259	676.0 676.0	0.73475 1.11419 13.37039	734.0 734.0	0.65644 0.82023 13.74325
KD4	1073.9 1073.9	1.33306 1.71922 17.80121	726.1 726.1	0.26856 0.67514 18.00862	804.6 804.6	0.17492 0.62628 18.47643
KD5	1124.2 1124.2	7.96826 7.54698 2.40076	791.3 791.3	3.70933 6.37462 11.20615	869.4 869.4	4.13342 6.56395 10.85012
KD6	1188.8 1188.8	1.34961 4.19350 13.52042	837.6 837.6	0.11772 2.91093 12.70470	916.1 916.1	0.18338 2.67184 13.02876
KD7	1250.9 1250.9	0.96958 2.10348 16.24552	890.6 890.6	1.35900 3.39114 13.68472	971.6 971.6	1.12420 2.82825 14.26726
KD8	1381.6 1381.6	0.28032 0.37074 19.07300	992.8 992.8	0.33039 0.70193 18.36999	1079.7 1079.7	0.32986 0.64924 18.51246

Table S14. Crystal field parameters of the ground J =15/2 multiplet. The quantization axis is the main magnetic axis g_Z of the ground Kramers doublet state.

Rank	Projection	Basis MB	Basis VDZP	Basis VTZP
	-2	-0.1406898E+01	-0.8561021E+00	-0.8786159E+00
	-1	0.1118154E+01	0.1295228E+01	0.1332869E+01
2	0	-0.6906373E+01	-0.4530497E+01	-0.5025004E+01
	+1	-0.1260091E+01	-0.1587283E+01	-0.1607720E+01
	+2	-0.1753370E+01	-0.1389810E+01	-0.1524162E+01
	-4	0.8970863E-02	0.4873385E-02	0.5015457E-02
	-3	0.8810626E-03	0.2773085E-02	0.2869582E-02
	-2	0.1024859E-02	-0.2507227E-03	-0.2651868E-03
	-1	-0.5029624E-02	-0.4870842E-02	-0.4732106E-02
4	0	-0.1432189E-01	-0.1290040E-01	-0.1352647E-01
	+1	0.2533359E-02	0.3939366E-02	0.3556880E-02
	+2	0.4819509E-02	0.4216436E-02	0.4482322E-02
	+3	-0.6999085E-02	-0.5671462E-02	-0.5834179E-02
	+4	0.9079277E-02	0.1073913E-01	0.1130900E-01
	-6	-0.2971856E-03	-0.2067538E-03	-0.2066009E-03
	-5	-0.2715206E-04	-0.3772506E-04	-0.3413795E-04
	-4	0.4526810E-04	0.2457250E-04	0.2286445E-04
	-3	-0.1400190E-04	-0.6694873E-05	-0.9344041E-05
	-2	0.3934682E-04	0.4314311E-04	0.4439047E-04
	-1	-0.4836257E-04	-0.7100198E-04	-0.7926762E-04
6	0	0.3507592E-04	0.2489681E-04	0.2522378E-04
	+1	0.1143543E-03	0.1238955E-03	0.1351147E-03
	+2	0.5186264E-05	-0.2581710E-06	-0.1186932E-06
	+3	-0.3300954E-04	-0.3545264E-04	-0.3756457E-04
	+4	0.5180304E-04	0.6681765E-04	0.6551242E-04
	+5	-0.2689489E-04	-0.5736221E-04	-0.5459312E-04
	+6	-0.9138532E-04	-0.2136203E-03	-0.2201531E-03

Table S15. Squared magnitudes of projections of the local ab initio CF eigenstates calculated for one Dy ion onto pseudospin eigenstates with pseudospin J = 15/2 and projection M_J, using VTZP results.

MJ	KD1		KD2		KD3		KD4	
-15/2	**6.47E-01**	**3.53E-01**	2.92E-07	4.12E-07	5.42E-05	9.96E-09	5.34E-06	3.61E-08
-13/2	9.52E-08	4.07E-08	**5.99E-01**	**3.86E-01**	9.87E-03	1.12E-05	4.72E-05	3.36E-04
-11/2	3.91E-05	2.12E-05	6.63E-03	4.50E-03	**8.49E-01**	1.73E-03	1.28E-02	1.68E-02
-9/2	1.82E-05	8.93E-06	6.94E-04	4.54E-04	**7.48E-02**	1.40E-04	8.09E-03	3.36E-03
-7/2	1.05E-04	5.69E-05	2.79E-04	1.19E-04	1.27E-02	6.20E-04	2.29E-02	1.60E-03
-5/2	9.30E-07	9.38E-07	6.44E-04	4.94E-04	1.08E-02	4.41E-03	2.31E-03	8.11E-02
-3/2	4.08E-05	2.36E-05	5.34E-05	2.38E-05	2.05E-03	3.73E-03	**3.13E-01**	5.63E-03
-1/2	2.68E-07	6.34E-07	8.75E-04	3.04E-04	1.42E-03	2.85E-02	2.92E-03	**5.29E-01**
+1/2	6.34E-07	2.68E-07	3.04E-04	8.75E-04	2.85E-02	1.42E-03	**5.29E-01**	2.92E-03
+3/2	2.36E-05	4.08E-05	2.38E-05	5.34E-05	3.73E-03	2.05E-03	5.63E-03	**3.13E-01**
+5/2	9.38E-07	9.30E-07	4.94E-04	6.44E-04	4.41E-03	1.08E-02	8.11E-02	2.31E-03
+7/2	5.69E-05	1.05E-04	1.19E-04	2.79E-04	6.20E-04	1.27E-02	1.60E-03	2.29E-02
+9/2	8.93E-06	1.82E-05	4.54E-04	6.94E-04	1.40E-04	**7.48E-02**	3.36E-03	8.09E-03
+11/2	2.12E-05	3.91E-05	4.50E-03	6.63E-03	1.73E-03	**8.49E-01**	1.68E-02	1.28E-02
+13/2	4.07E-08	9.52E-08	**3.86E-01**	**5.99E-01**	1.12E-05	9.87E-03	3.36E-04	4.72E-05
+15/2	**3.53E-01**	**6.47E-01**	4.12E-07	2.92E-07	9.96E-09	5.42E-05	3.61E-08	5.34E-06

MJ	KD5		KD6		KD7		KD8	
-15/2	1.33E-05	5.07E-06	2.11E-06	3.16E-05	6.63E-05	2.88E-05	8.18E-05	2.74E-05
-13/2	7.91E-04	2.44E-04	9.57E-04	4.90E-04	1.19E-03	1.59E-04	2.97E-04	6.71E-04
-11/2	9.00E-03	1.04E-02	9.10E-03	3.97E-02	1.97E-03	1.92E-02	8.31E-03	1.06E-02
-9/2	**1.44E-01**	**1.45E-01**	1.81E-02	**1.73E-01**	8.98E-02	**1.89E-01**	5.23E-02	**1.00E-01**
-7/2	**1.72E-01**	4.61E-02	2.36E-02	3.73E-02	**1.57E-01**	**1.90E-01**	**2.22E-01**	**1.13E-01**
-5/2	1.49E-03	9.80E-02	**3.24E-01**	6.87E-02	**1.49E-01**	1.75E-02	3.46E-02	**2.07E-01**
-3/2	**1.21E-01**	6.82E-02	3.96E-02	**2.23E-01**	4.87E-02	2.91E-02	**1.14E-01**	3.21E-02
-1/2	6.43E-02	**1.19E-01**	1.74E-02	2.51E-02	8.68E-02	2.01E-02	1.85E-02	8.58E-02
+1/2	**1.19E-01**	6.43E-02	2.51E-02	1.74E-02	2.01E-02	8.68E-02	8.58E-02	1.85E-02
+3/2	6.82E-02	**1.21E-01**	**2.23E-01**	3.96E-02	2.91E-02	4.87E-02	3.21E-02	**1.14E-01**
+5/2	9.80E-02	1.49E-03	6.87E-02	**3.24E-01**	1.75E-02	**1.49E-01**	**2.07E-01**	3.46E-02
+7/2	4.61E-02	**1.72E-01**	3.73E-02	2.36E-02	**1.90E-01**	**1.57E-01**	**1.13E-01**	**2.22E-01**
+9/2	**1.45E-01**	**1.44E-01**	**1.73E-01**	1.81E-02	**1.89E-01**	8.98E-02	**1.00E-01**	5.23E-02
+11/2	1.04E-02	9.00E-03	3.97E-02	9.10E-03	1.92E-02	1.97E-03	1.06E-02	8.31E-03
+13/2	2.44E-04	7.91E-04	4.90E-04	9.57E-04	1.59E-04	1.19E-03	6.71E-04	2.97E-04
+15/2	5.07E-06	1.33E-05	3.16E-05	2.11E-06	2.88E-05	6.63E-05	2.74E-05	8.18E-05

Magnetic exchange

Magnetic exchange computed by BS-DFT method using ORCA 5.0.3 quantum chemistry software. Computationally, the Dy(III) was modeled by Gd(III) since the latter has a non-degenerate ground state ^{8}S term, whereas the applicability of the DFT method for the Dy(III), which has a near-degenerate ground state, ^{6}H term, is questionable. The calculations were done using several density functionals. The obtained magnetic exchange were transformed to the Ising model, by the formula:

$$H_{BS-DFT} = -2J_{DFT\ on\ Gd} \times \frac{7}{2} \times \frac{7}{2} = -J_{Lines} \times \frac{5}{2} \times \frac{5}{2} = -J_{Ising} \times \frac{1}{2} \times \frac{1}{2}$$

$$J_{Ising} = 98 \times J_{DFT\ on\ Gd}$$

$$J_{Lines} = \frac{98}{25} \times J_{DFT\ on\ Gd}$$

In the manuscript, another Hamiltonian is employed, $H_{exch} = -2Jm_{JA}m_{JB}$, where $m_{JA} = m_{JB} = 15/2$. The parameter of magnetic interaction for this Hamiltonian is obtained as follows:

$$J = \frac{49}{225} \times J_{DFT\ on\ Gd} = \frac{1}{18} \times J_{Lines} = \frac{1}{450} \times J_{Ising}$$

Table S16. Magnetic exchange obtained in BS-DFT calculations as well as those obtained in POLY_ANISO (in cm^{-1}).

DFT functional	Magnetic exchange $J_{DFT\ on\ Gd}$ for Hamiltonian $H = -2JS_AS_B$, where $S_A = S_B = 7/2$	Rescaled magnetic exchange J_{Lines} for Hamiltonian $H = -JS_AS_B$, where $S_A = S_B = 5/2$	Rescaled magnetic exchange J_{Ising} for Ising Hamiltonian $H = J_{Ising}\tilde{s}_{Az}\tilde{s}_{Bz}$, where $s_A = s_B = 1/2$	Rescaled magnetic exchange J for the Hamiltonian $H = -2Jm_{JA}m_{JB}$, where $m_{JA} = m_{JB} = 15/2$
3LYP	-0.013437227	-0.052673928	-1.316848200	-0.002926329
CAM-B3LYP	-0.013437254	-0.052674035	-1.316850887	-0.002926335
wB97	-0.013437227	-0.052673928	-1.316848200	-0.002926329
RI-B2PLYP	-0.013437254	-0.052674035	-1.316850887	-0.002926335
LC-PBE	-0.013437254	-0.052674035	-1.316850887	-0.002926335
TPSS0	-0.017916339	-0.070232047	-1.755801183	-0.003901780
magnetic exchange obtained in POLY_ANISO (cm^{-1})				
		Lines model	Ising model	
exchange-only (fitted)	--	-0.035634602	-0.890865057	-0.001979700
dipole-dipole only (not fitted)	--	-0.062361936	-1.559048404	-0.003464552
total magnetic interaction	--	-0.097996538	-2.449913461	-0.005444252

Exchange and Zeeman interactions in Dy_2

From Figures 4 and S19, the magnetic field required for the magnetic state to become ground state was estimated to be around ± 0.15 T. We can use this value to estimate the magnetic exchange as follows.

Derivation of the energy gap between ferromagnetic and antiferromagnetic states in the absence of applied magnetic field. This is done by using the Ising exchange Hamiltonian:

$$H_{exch} = -J_{Ising}\tilde{s}_{1z}\tilde{s}_{2z}$$

The $\tilde{s}_{1z}$ and $\tilde{s}_{2z}$ are the pseudospins of the ground KD on each Dy sites. They can take values of $\pm\frac{1}{2}$ each. There are 4 coupled states and the energy of each state is:

$$E_{++} = -J_{Ising}\left(+\frac{1}{2}\right)\left(+\frac{1}{2}\right) = -\frac{1}{4}J_{Ising}$$
$$E_{+-} = -J_{Ising}\left(+\frac{1}{2}\right)\left(-\frac{1}{2}\right) = +\frac{1}{4}J_{Ising}$$
$$E_{-+} = -J_{Ising}\left(-\frac{1}{2}\right)\left(+\frac{1}{2}\right) = +\frac{1}{4}J_{Ising}$$
$$E_{--} = -J_{Ising}\left(-\frac{1}{2}\right)\left(-\frac{1}{2}\right) = -\frac{1}{4}J_{Ising}$$

As we see, there are two groups, doubly degenerate: $E_{++} = E_{--}$ and $E_{+-} = E_{-+}$.
The energy splitting between the two groups is:

$$\Delta E = E_{++} - E_{+-} = -\frac{1}{4}J_{Ising} - \left(\frac{1}{4}J_{Ising}\right) = -\frac{1}{2}J_{Ising}$$

Since the $J_{Ising} < 0$, the ground state is antiferromagnetic, $\Delta E > 0$.
From *ab initio* calculations, $\Delta E \sim 1.225\ cm^{-1}$, which corresponds to an Ising exchange of $J_{Ising} = -2\Delta E = -2.45\ cm^{-1}$. Correspondingly,

$$J_{Lines} = \frac{1}{25}J_{Ising}$$

Now, this energy gap is compensated by the Zeeman splitting of the excited doublet state E_{++}, E_{--}. The ground state has no net magnetic moment and therefore, does not interact with applied magnetic field and remains degenerate.

State	magnetic moment on site 1	magnetic moment on site 2	total magnetic moment (sum of two contributions)
++	$\mu_B g_J M_J = 10\mu_B$	$\mu_B g_J M_J = 10\mu_B$	$2\mu_B g_J M_J = 20\mu_B$
+-	$\mu_B g_J M_J = 10\mu_B$	$\mu_B g_J M_J = -10\mu_B$	$0\mu_B$
-+	$\mu_B g_J M_J = -10\mu_B$	$\mu_B g_J M_J = 10\mu_B$	$0\mu_B$
--	$\mu_B g_J M_J = -10\mu_B$	$\mu_B g_J M_J = -10\mu_B$	$2\mu_B g_J M_J = -20\mu_B$

Each of the above four states interacts with magnetic field, via Zeeman interaction, and their energy changes as follows:

State	total magnetic moment (sum of two contributions)	Energy in applied magnetic field of strength H ($H_{Zee} = \mu H$)
++	$2\mu_B g_J M_J = 20\mu_B$	$20\mu_B H$
+-	$0\mu_B$	$0\mu_B H$
-+	$0\mu_B$	$0\mu_B H$
--	$2\mu_B g_J M_J = -20\mu_B$	$-20\mu_B H$

At level crossing the Zeeman energy compensates the antiferromagnetic exchange splitting ΔE and therefore, we have the relationship:

$$\Delta E = -\frac{1}{2} J_{Ising} = 2\mu_B g_J M_J H = 20\mu_B H$$

Form this relationship, we extract J_{Ising}:

$$J_{Ising} = -4\mu_B g_J M_J H = -40\mu_B H$$

Using the $g_J = \frac{4}{3}$ and $M_J = \frac{15}{2}$ and $H = 0.15\,T$ and $\mu_B = 0.4668643740\ cm^{-1}/T$ we have:

$$J_{Ising} = -4 \times 0.4668643740 \times \frac{4}{3} \times \frac{15}{2} \times 0.15 = -2.8011862\ cm^{-1}$$

$$J_{Lines} = \frac{1}{25} J_{Ising} = -\frac{2.8011862}{25} = -0.1120474\ cm^{-1}$$

Comparison with ab initio results:
From *ab initio* calculations, $\Delta E = 1.225\ cm^{-1}$, which corresponds to an Ising exchange of $J_{Ising} = -2\Delta E = -2.45\ cm^{-1}$. The corresponding Lines parameter (of total magnetic interaction, exchange + dipolar) is:

$$J_{Lines} = \frac{1}{25} J_{Ising} = -0.098\ cm^{-1}$$

Dipolar-dipolar interaction in Dy_2 using Hamiltonian $H = -2Jm_{JA}m_{JB}$, where $m_{JA} = m_{JB} = 15/2$

For a centrosymmetric dinuclear Dy(III) system, the intramolecular dipolar-dipolar interaction can be calculated by the following equation:[21-24]

$$E_{dip} = -\left\{\frac{\mu_0}{4\pi}\right\}\frac{\mu_1\mu_2}{r^3}[3\cos^2\theta - 1]$$

Using SI units:

$\mu_0 = 4\pi \times 10^{-7}$ Henry/meter = Tesla x meter/Ampere = [kg·m·s^{-2}·A^{-2}]

$\mu_B = 9.274 \times 10^{-24}$ Joule/Tesla = [kg m^2 s^{-2} / kg s^{-2} A^{-1}]=[A m^2]

$r_{12} = 4.779 \times 10^{-10}$ meter

θ = 87.6°

On-site magnetic moment

$$\mu_1 = \mu_2 = -\mu_B g_Z s_Z = -\mu_B \times 20 \times \left(\pm\frac{1}{2}\right) = \mp 10\mu_B \text{ (along Z direction)}$$

Therefore, $\Delta E_{dip} = 0.7932\ cm^{-1}$

Writing only the dipolar(+exchange) term and Zeeman term of a two ion Ising Hamiltonian (m_J = ±15/2 with large ZFS), with the assumption that field is along Z direction (easy axis) and dominant interaction is also along Z direction.

$H_{dip+Zeeman}$ = $\mu_B g_{zz} B_z m_{JA} + \mu_B g_{zz} B_z m_{JB} + 2J_{zz} m_{JA} m_{JB} = \mu_B g B_z m_{JA} + \mu_B g B_z m_{JB} + 2J m_{JA} m_{JB}$, here $m_{JA} = m_{JB} = \pm 15/2$

Gap between AFM and FM states at zero field:

$\Delta E = 2J(+15/2)(+15/2) - 2J(+15/2)(-15/2) = 4J(15/2)^2 = 4Jm_J^2$ with m_J = 15/2 or -15/2)

For our case, $\underline{4}J(15/2)^2 = 0.7932$ cm^{-1}. So, J should be = 0.0035 cm^{-1}, very similar to micro-SQUID results (see below, calculation of J from H_{ex}).

Derivation of H_{ex}:

At $B_z = H_{ex}$, the FM and AFM states cross, i.e.,

$E_{FM} = E_{AFM}$

$\mu_B g H_{ex}(15/2) + \mu_B g H_{ex}(15/2) + 2J(15/2)*(15/2) = \mu_B g H_{ex}(15/2) + \mu_B g H_{ex}(-15/2) + 2J(15/2)*(-15/2)$

Therefore, $H_{ex} = -2Jm_J/g_J\mu_B$

For our case, H_{ex} = 0.15 T, m_J = 15/2, g = 4/3. Hence, J = 0.0062 cm^{-1}.

Table S17. Energies of the exchange states (cm^{-1}) for **Dy_2** as obtained in POLY_ANISO.

Low-lying exchange states				
Coupled State	Exchange	Dipole-Dipole	Total	Total, relative
1	-0.222717121924	-0.389767194186	-0.612484456534	0.000000000000
2	-0.222717121676	-0.389767190194	-0.612484452796	0.000000003737
3	0.222715401282	0.389757027632	0.612474692552	1.224959149086
4	0.222715403176	0.389757029605	0.612474692625	1.224959149158
5	436.864043843841	436.729990224003	436.559647788245	437.172132244779
6	436.864043856900	436.729990374080	436.559647852568	437.172132309101
7	436.940241774090	436.781221087511	436.584615150340	437,197099606874
8	436.940241796091	436.781221164348	436.584615321111	437.197099777645
..	…	…	…	…

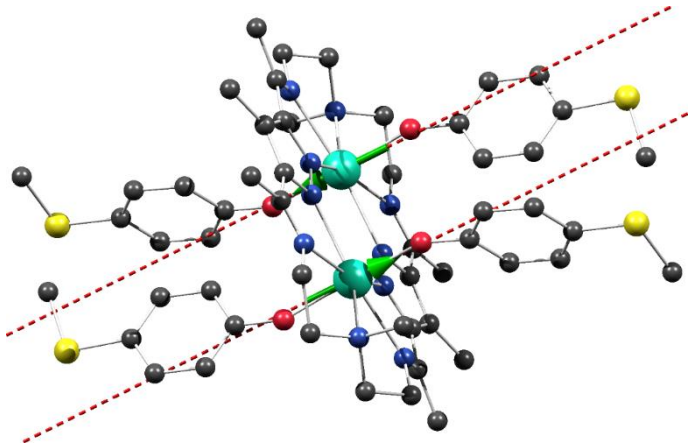

Figure S20. Orientation of main magnetic axes in **Dy_2** with respect to the molecular frame, using the VTZP results.

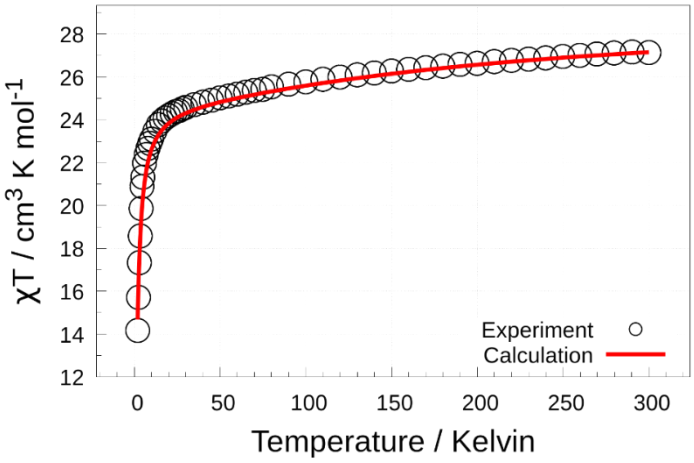

Figure S21. Comparison between measured and calculated magnetic susceptibility.

5. References

1. Sachse, A.; Penkova, L.; Noël, G.; Dechert, S.; Varzatskii, O. A.; Fritsky, I. O.; Meyer, F., Efficient Syntheses of Some Versatile 3,5-Bifunctional Pyrazole Building Blocks. *Synthesis* **2008,** *2008*, 800-806.
2. Wu, J.; Demeshko, S.; Dechert, S.; Meyer, F., Macrocycle based dinuclear dysprosium(III) single molecule magnets with local D_{5h} coordination geometry. *Dalton Trans.* **2021,** *50*, 17573-17582.
3. Sheldrick, G. M., Crystal structure refinement with *SHELXL*. *Acta Crystallogr., Sect. C: Struct. Chem.* **2015,** *71*, 3-8.
4. Sheldrick, G. M., *SHELXT* - integrated space-group and crystal-structure determination. *Acta Crystallogr., Sect. A: Found. Adv.* **2015,** *71*, 3-8.
5. Dolomanov, O. V.; Bourhis, L. J.; Gildea, R. J.; Howard, J. A. K.; Puschmann, H., *OLEX2*: a complete structure solution, refinement and analysis program. *J. Appl. Crystallogr.* **2009,** *42*, 339-341.
6. Casanova, D.; Cirera, J.; Llunell, M.; Alemany, P.; Avnir, D.; Alvarez, S., Minimal Distortion Pathways in Polyhedral Rearrangements. *J. Am. Chem. Soc.* **2004,** *126*, 1755-1763.
7. Pinsky, M.; Avnir, D., Continuous Symmetry Measures. 5. The Classical Polyhedra. *Inorg. Chem.* **1998,** *37*, 5575-5582.
8. Bain, G. A.; Berry, J. F., Diamagnetic Corrections and Pascal's Constants. *J. Chem. Educ.* **2008,** *85*, 532.
9. Wu, H.; Li, M.; Xia, Z.; Montigaud, V.; Cador, O.; Le Guennic, B.; Ke, H.; Wang, W.; Xie, G.; Chen, S.; Gao, S., High temperature quantum tunnelling of magnetization and thousand kelvin anisotropy barrier in a Dy_2 single-molecule magnet. *Chem. Commun.* **2021,** *57*, 371-374.
10. Zhang, B.; Zhou, Y.; Hu, R.-H.; Hu, H.-S.; Chen, L.; Chen, S.-Y.; Zhang, Y.-Q.; Li, Z.-Y.; Englert, U., High-Coordinated Dy_2 Single-Molecule Magnet with an Anistropy Barrier Exceeding 700 K. *Cryst. Growth Des.* **2024,** *24*, 3370-3377.
11. Li, M.; Wu, H.; Xia, Z.; Montigaud, V.; Cador, O.; Le Guennic, B.; Ke, H.; Wang, W.; Xie, G.; Chen, S., Bromine-bridged Dy_2 single-molecule magnet: magnetic anisotropy driven by cis/trans stereoisomers. *Chem. Commun.* **2019,** *55*, 14661-14664.
12. Liu, F.; Krylov, D. S.; Spree, L.; Avdoshenko, S. M.; Samoylova, N. A.; Rosenkranz, M.; Kostanyan, A.; Greber, T.; Wolter, A. U. B.; Büchner, B.; Popov, A. A., Single molecule magnet with an unpaired electron trapped between two lanthanide ions inside a fullerene. *Nat. Commun.* **2017,** *8*, 16098.
13. Liu, F.; Velkos, G.; Krylov, D. S.; Spree, L.; Zalibera, M.; Ray, R.; Samoylova, N. A.; Chen, C.-H.; Rosenkranz, M.; Schiemenz, S.; Ziegs, F.; Nenkov, K.; Kostanyan, A.; Greber, T.; Wolter, A. U. B.; Richter, M.; Büchner, B.; Avdoshenko, S. M.; Popov, A. A., Air-stable redox-active nanomagnets with lanthanide spins radical-bridged by a metal-metal bond. *Nat. Commun.* **2019,** *10*, 571.
14. Wang, Y.; Velkos, G.; Israel, N. J.; Rosenkranz, M.; Büchner, B.; Liu, F.; Popov, A. A., Electrophilic Trifluoromethylation of Dimetallofullerene Anions en Route to Air-Stable Single-Molecule Magnets with High Blocking Temperature of Magnetization. *J. Am. Chem. Soc.* **2021,** *143*, 18139-18149.

15. Velkos, G.; Krylov, D. S.; Kirkpatrick, K.; Spree, L.; Dubrovin, V.; Büchner, B.; Avdoshenko, S. M.; Bezmelnitsyn, V.; Davis, S.; Faust, P.; Duchamp, J.; Dorn, H. C.; Popov, A. A., High Blocking Temperature of Magnetization and Giant Coercivity in the Azafullerene $Tb_2@C_{79}N$ with a Single-Electron Terbium–Terbium Bond. *Angew. Chem., Int. Ed.* **2019,** *58*, 5891-5896.
16. Demir, S.; Gonzalez, M. I.; Darago, L. E.; Evans, W. J.; Long, J. R., Giant coercivity and high magnetic blocking temperatures for N_2^{3-} radical-bridged dilanthanide complexes upon ligand dissociation. *Nat. Commun.* **2017,** *8*, 2144.
17. Gould, C. A.; Mu, E.; Vieru, V.; Darago, L. E.; Chakarawet, K.; Gonzalez, M. I.; Demir, S.; Long, J. R., Substituent Effects on Exchange Coupling and Magnetic Relaxation in 2,2'-Bipyrimidine Radical-Bridged Dilanthanide Complexes. *J. Am. Chem. Soc.* **2020,** *142*, 21197-21209.
18. Fdez. Galván, I.; Vacher, M.; Alavi, A.; Angeli, C.; Aquilante, F.; Autschbach, J.; Bao, J. J.; Bokarev, S. I.; Bogdanov, N. A.; Carlson, R. K.; Chibotaru, L. F.; Creutzberg, J.; Dattani, N.; Delcey, M. G.; Dong, S. S.; Dreuw, A.; Freitag, L.; Frutos, L. M.; Gagliardi, L.; Gendron, F.; Giussani, A.; González, L.; Grell, G.; Guo, M.; Hoyer, C. E.; Johansson, M.; Keller, S.; Knecht, S.; Kovačević, G.; Källman, E.; Li Manni, G.; Lundberg, M.; Ma, Y.; Mai, S.; Malhado, J. P.; Malmqvist, P. Å.; Marquetand, P.; Mewes, S. A.; Norell, J.; Olivucci, M.; Oppel, M.; Phung, Q. M.; Pierloot, K.; Plasser, F.; Reiher, M.; Sand, A. M.; Schapiro, I.; Sharma, P.; Stein, C. J.; Sørensen, L. K.; Truhlar, D. G.; Ugandi, M.; Ungur, L.; Valentini, A.; Vancoillie, S.; Veryazov, V.; Weser, O.; Wesołowski, T. A.; Widmark, P.-O.; Wouters, S.; Zech, A.; Zobel, J. P.; Lindh, R., OpenMolcas: From Source Code to Insight. *J. Chem. Theory Comput.* **2019,** *15*, 5925-5964.
19. Aquilante, F.; Autschbach, J.; Carlson, R. K.; Chibotaru, L. F.; Delcey, M. G.; De Vico, L.; Fdez. Galván, I.; Ferré, N.; Frutos, L. M.; Gagliardi, L.; Garavelli, M.; Giussani, A.; Hoyer, C. E.; Li Manni, G.; Lischka, H.; Ma, D.; Malmqvist, P. Å.; Müller, T.; Nenov, A.; Olivucci, M.; Pedersen, T. B.; Peng, D.; Plasser, F.; Pritchard, B.; Reiher, M.; Rivalta, I.; Schapiro, I.; Segarra-Martí, J.; Stenrup, M.; Truhlar, D. G.; Ungur, L.; Valentini, A.; Vancoillie, S.; Veryazov, V.; Vysotskiy, V. P.; Weingart, O.; Zapata, F.; Lindh, R., Molcas 8: New capabilities for multiconfigurational quantum chemical calculations across the periodic table. *J. Comput. Chem.* **2016,** *37*, 506-541.
20. Roos, B. O.; Lindh, R.; Malmqvist, P.-Å.; Veryazov, V.; Widmark, P.-O.; Borin, A. C., New Relativistic Atomic Natural Orbital Basis Sets for Lanthanide Atoms with Applications to the Ce Diatom and LuF_3. *J. Phys. Chem. A* **2008,** *112*, 11431-11435.
21. Panissod, P.; Drillon, M., Magnetic Ordering due to Dipolar Interaction in Low Dimensional Materials. In *Magnetism: Molecules to Materials IV*, Wiley-VCH Verlag GmbH & Co. KGaA, 2001, pp 233-270.
22. Leng, J.-D.; Liu, J.-L.; Lin, W.-Q.; Gómez-Coca, S.; Aravena, D.; Ruiz, E.; Tong, M.-L., Unprecedented ferromagnetic dipolar interaction in a dinuclear holmium(III) complex: a combined experimental and theoretical study. *Chem. Commun.* **2013,** *49*, 9341-9343.
23. Guo, M.; Zhang, Y.-Q.; Zhu, Z.; Tang, J., Dysprosium Compounds with Hula-Hoop-like Geometries: The Influence of Magnetic Anisotropy and Magnetic

Interactions on Magnetic Relaxation. *Inorg. Chem.* **2018,** *57*, 12213-12221.
24. Bernbeck, M. G.; Orlova, A. P.; Hilgar, J. D.; Gembicky, M.; Ozerov, M.; Rinehart, J. D., Dipolar Coupling as a Mechanism for Fine Control of Magnetic States in ErCOT-Alkyl Molecular Magnets. *J. Am. Chem. Soc.* **2024,** *146*, 7243-7256.